Korean J. Chem. Eng., 39(11), 3165-3176 (2022)
DOI: 10.1007/s11814-022-1234-9

pISSN: 0256-1115
eISSN: 1975-7220

Experimental and numerical simulation study on the hydrodynamic characteristics of spherical and irregular-shaped particles in a 3D liquid-fluidized bed

Jian Peng*, Wei Sun*, Haisheng Han*,†, Le Xie,†, and Yao Xiao***

*School of Minerals Processing and Bioengineering, Central South University, Changsha 410083, China
**College of Chemistry and Chemical Engineering, Central South University, Changsha 410083, China
(*Received 12 June 2022 • Accepted 19 July 2022*)

Abstract−Recently, the fluidized bed has been shown to assist in improving the recovery of coarse minerals during flotation. In this study, the fluidization characteristics of spherical and irregular particles in a three-dimensional liquid-solid fluidized bed were studied by combining experimental and computational fluid dynamics (CFD) methods. Fluidization experiments were performed to investigate the effect of superficial velocity, particle shape, and particle size on solid holdup and bed expansion height. CFD model coupled different drag models for spherical and irregular particles were developed and validated by the experimental data of bed expansion ratio and pressure drop. Based on 3D CFD simulations, the axial and radial direction distributions of solid holdup, axial velocity, as well as granular temperature were obtained. Their distribution characteristics were analyzed and discussed in detail. The reported experimental data and simulation results can improve the understanding of irregular granular liquid-solid fluidized bed and provide a basis for further research on fluidized bed flotation.

Keywords: Fluidization, Irregular Particles, Multiphase Flow, Liquid-solid Fluidized Bed, Computational Fluid Dynamics (CFD)

INTRODUCTION

Considering the superior characteristics of the liquid-solid fluidized bed, such as high fluid-solid coupling and high heat and mass transfer performance, this method has been widely applied in diverse industries, including hydrometallurgy, extraction, and wastewater treatment [1-8]. Based on the concept of fluidized-bed flotation (FBF), HydroFloat and NovaCell were proposed to improve the separation and recovery performance of coarse particles (425-1180 microns) in the mineral processing industry [2,9-11].

Generally, the low recovery rate of coarse particles originates from inefficient separation caused by excessive turbulence in conventional mechanical flotation cells. Compared with conventional mechanical agitation flotation devices, fluidized-bed flotation provides an appropriate turbulent environment and favorable hydrodynamic conditions to recover coarse particles [12,13]. Accordingly, it is of significant importance to adjust the affecting parameters in the fluidized-bed flotation. However, it is an enormous challenge to study the interaction between liquid, solid, and gas phases in turbulent flows. Meanwhile, a highly turbulent environment may adversely affect the recovery rate of coarse particles [14,15]. In order to resolve this problem, it is necessary to set appropriate parameters for flow velocity and size, shape, and density of particles before introducing bubbles into the fluidized-bed flotation machine.

Reviewing the literature indicates that numerous experimental and numerical investigations have been carried out to analyze liquid-particle interactions during fluidization using [16-20]. Most studies assume that all particles are spherical; however, in practical engineering applications, particles may have different shapes and are rarely completely spherical. Therefore, it is of great significance to investigate the hydrodynamics of irregular particles in fluidized beds to analyze fluidization flotation more accurately and design efficient operations.

Since the advent of numerical simulations, CFD has been widely adopted as one of the most effective modeling tools to study complex liquid-particle flow phenomena in fluidized bed systems [17,21-26]. Generally, the proposed CFD models for fluidized beds can be mainly classified into two categories, including the Euler-Lagrange and the Euler-Euler models. In the former model, equations of motion are solved for each particle. Accordingly, particle-particle collisions and the applied forces are considered for each particle separately [27,28], but the calculation cost is relatively high. In the Euler-Euler two-fluid model, liquid and solid phases are considered to be interconnected and continuous. To achieve closure, the kinetic theory of granular flow (KTGF) is used to model the viscosity and pressure of the solid phase. The Euler-Euler two-fluid model coupled with the KTGF has relatively low computational expenses, so this model has been widely used to calculate solid flow characteristics [29-33].

The main objective of the present study is to explore the hydrodynamic properties of liquid-particle fluidized beds, considering spherical and irregular particles. To this end, the influence of numerous parameters, such as particle size, shape, and superficial liquid velocity of particles, was analyzed on the bed expansion and pressure drop of a three-dimensional (3D) fluidized bed. Meanwhile, the Euler-Euler model coupled with different drag models was validated. Then the established model was employed to explore the hydrodynamic behavior of liquid-particle fluidized beds, including the solid holdup,

†To whom correspondence should be addressed.
E-mail: hanhai5086@csu.edu.cn, xiele2018@csu.edu.cn

axial velocity, and granular temperature. The present study is expected to improve the understanding of irregular particle fluidization and provide a basis to design the fluidized flotation.

EXPERIMENTAL DESIGN AND PROCEDURES

1. Test Setup and Operating Conditions

Fig. 1(a) shows the configuration of the experimental setup of a fluidized bed that has a 50 mm diameter and 500 mm high transparent plexiglass for direct observation. A circular distributor with an open hole ratio of 18% and an aperture of 1 mm is arranged at the bottom of the fluidized bed. During the experiment, spherical and irregular glass beads operate as a solid phase, while water operates as the fluidization medium. Before the experiment, irregular glass beads were obtained using a conical ball mill (XMQ-240×90, Wuhan Exploration Machinery Factory, China). It should be indi-

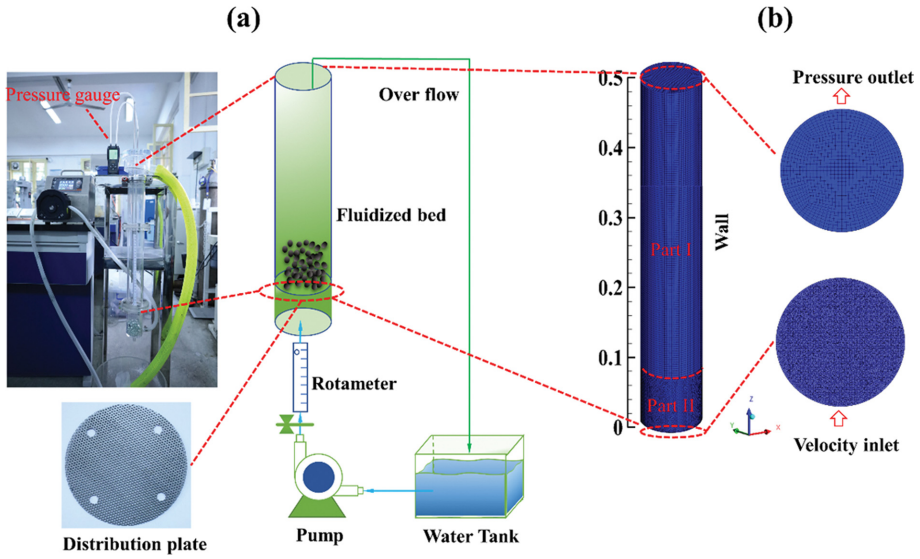

Fig. 1. Configuration of the liquid-solid fluidized bed experimental setup.

Table 1. Experimental parameters and results

Parameters	Liquid phase					Particle phase			
	Flow rate (L/min)	Density (kg/m^3)	Viscosity (kg/(m·s))	Superficial liquid velocity (m/s)	Ratio of velocity to min velocity (-)	Density (kg/m^3)	Diameter (mm)	Degree of expansion (%)	Particle shape
1#	2.0	998.2	0.001	0.017	6.85	2,670	0.5±0.1	50.0	Spherical particles
2#	2.5	998.2	0.001	0.0212	8.54	2,670	0.5±0.1	67.0	
3#	3.0	998.2	0.001	0.0255	10.27	2,670	0.5±0.1	86.0	
4#	3.5	998.2	0.001	0.0297	11.96	2,670	0.5±0.1	106.0	
5#	4.0	998.2	0.001	0.034	13.70	2,670	0.5±0.1	145.0	
6#	2.0	998.2	0.001	0.017	6.85	2,670	0.5±0.1	70.0	Irregular particles
7#	2.5	998.2	0.001	0.0212	8.54	2,670	0.5±0.1	95.0	
8#	3.0	998.2	0.001	0.0255	10.27	2,670	0.5±0.1	124.0	
9#	3.5	998.2	0.001	0.0297	11.96	2,670	0.5±0.1	155.0	
10#	4.0	998.2	0.001	0.034	13.70	2,670	0.5±0.1	190.0	
11#	3.0	998.2	0.001	0.0255	5.24	2670	0.7±0.1	53.0	Spherica particles
12#	3.5	998.2	0.001	0.0297	6.10	2670	0.7±0.1	68.0	
13#	4.0	998.2	0.001	0.034	6.99	2670	0.7±0.1	81.0	
14#	4.5	998.2	0.001	0.0382	7.85	2670	0.7±0.1	94.0	
15#	5.0	998.2	0.001	0.0425	8.74	2670	0.7±0.1	108.0	
16#	3.0	998.2	0.001	0.0255	5.24	2670	0.7±0.1	66.0	Irregular particles
17#	3.5	998.2	0.001	0.0297	6.10	2670	0.7±0.1	82.0	
18#	4.0	998.2	0.001	0.034	6.99	2670	0.7±0.1	99.0	
19#	4.5	998.2	0.001	0.0382	7.85	2670	0.7±0.1	121.0	
20#	5.0	998.2	0.001	0.0425	8.74	2670	0.7±0.1	139.0	

cated that four different glass bead samples were used in this study in the fluidization tests.

The main steps of each experiment can be summarized as follows. In the first step, spherical or irregular glass beads were placed on the distribution plate with an initial filling height of 100 mm. Then a peristaltic pump (WT600-3J, Chang Precision Pump Co., China) with a flow error of less than 0.5% was turned on to convey water to the bottom of the fluidized bed. The pump speed was adjusted according to the required inlet speed at the bottom of the fluidized bed. When the superficial velocity of water exceeds the minimum fluidization velocity, the glass beads leave the distribution plate and suspend in the fluidized bed. When particle fluidization reaches the steady-state condition, the bed expansion height is recorded. Each data was measured three times and the average value was recorded. Experimental parameters and results are shown in Table 1. The bed expansion ratio can be defined in the form below:

$$\chi = \frac{H_e - H_i}{H_i} \times 100\% \quad (1)$$

where χ is the bed expansion ratio, H_i is the initial bed height, and H_e is the bed height after fluidization.

In addition, the pressure drop continues to fluctuate with flow time when a quasi-steady state is obtained. In this study, three sections were used at Z=100 mm, 150 mm, and 200 mm to record the time evolution of the pressure drop. The differential pressure gauge (Sima AS510, China) consists of two copper tubes, a digital display pressure gauge, and a rubber hose. Accuracy and resolution of the pressure gauge are ±3 Pa and ±1 Pa, respectively. When measuring the pressure drop, the digital differential pressure meter directly reads the pressure drop at the ends of two copper tubes. The data sampling rate is 120 Hz and the measurement is performed for 30 seconds. Distilled water with a density of 998.2 kg/m^3 and a viscosity of 0.001 Pa s was used as a fluidization medium. All experiments were conducted in a room with a temperature of 20 °C.

Table 1 shows the experimental data of the bed expansion ratio for a liquid-solid fluidized bed with two particle sizes (0.5±0.1 mm and 0.7±0.1 mm), particle density of 2,670 kg/m^3, and different superficial liquid velocities. The labels 1-5# and 11-15# refer to spherical particles, while the labels 6-10# and 16-20# refer to irregular particles.

2. Calculating the Sphericity and Shape Factor of Particles

The present study used the following three methods to determine the size of particles: classical sieving analysis (24-mesh, 30-mesh, 45-mesh sieve), optical microscopy (GX-6, Beijing Jing Bai Zhuo Xian Technology Co., China), and static image analysis using Image-Pro software. Fig. 2 illustrates the distribution of the particle size the particle morphology.

The sphericity ψ of a particle refers to the ratio of the surface area of a perfect sphere with the same volume to the surface area of the particle. Based on this definition, spherical particles have a sphericity of 1, while irregular particles vary in the range of $0<\psi<1$, which can

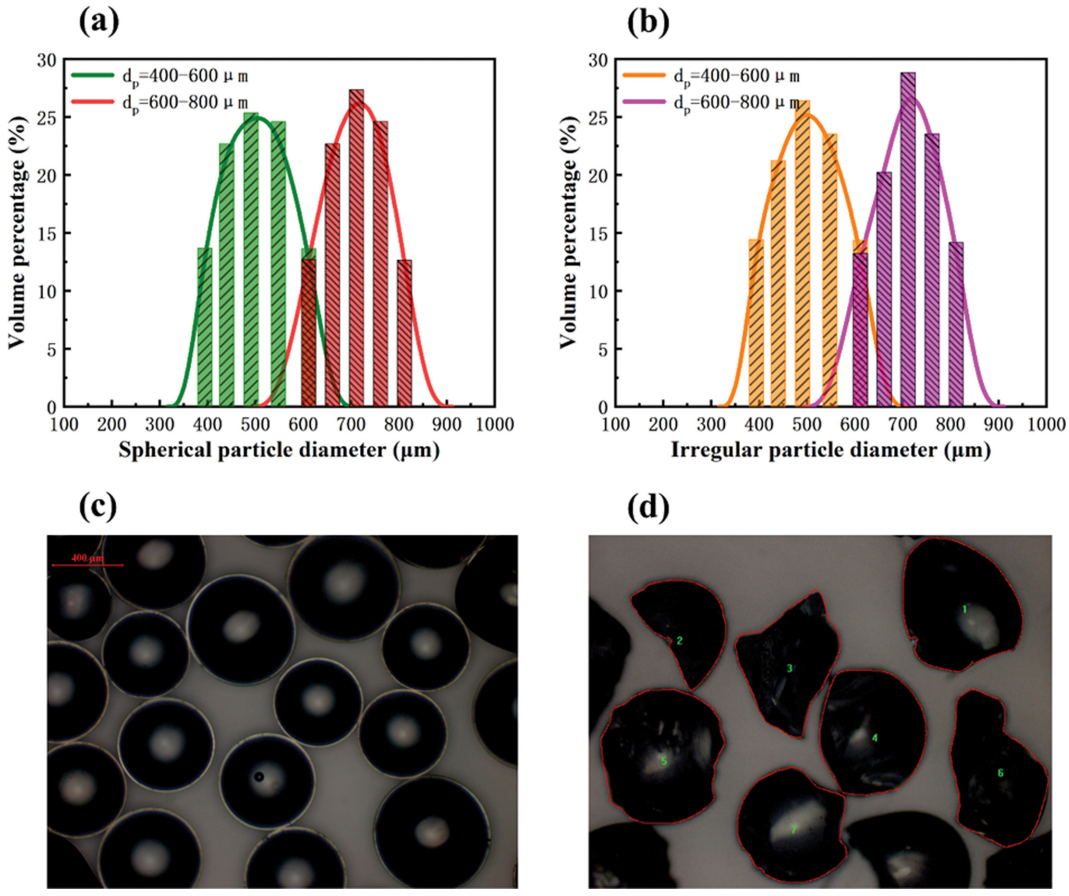

Fig. 2. (a), (b) Distribution of the particle size; (c), (d) Morphology of particles under an optical microscope.

be determined using image analysis [34,35]. Accordingly, numerous images were captured using an optical microscope, and then they were analyzed in Image-Pro software. The shape factor and roundness P_R of particles can be obtained using the following equations:

$$\psi = \frac{4\pi A}{L^2} \tag{2}$$

$$P_R = \frac{4A}{\pi Z^2} \tag{3}$$

where A and L are the actual area and perimeter of the irregular particle, respectively, and Z is the maximum distance of the particle from one edge to the other. In most captured images, $0.624 < \psi < 0.973$ and $0.411 < P_R < 0.971$. The mean value of the shape factor is 0.83.

CFD MODELING AND SIMULATION METHOD

To simulate liquid-particle interaction, it is necessary to consider the liquid flow and motions of particles. To this end, an Euler-Euler liquid-solid model was employed to analyze the fluidization characteristics of glass beads particles. The governing equations are the continuity and momentum equations. Kinetic theory of granular flow (KTGF), turbulent, standard Gidaspow, and the modified Gidaspow models were applied to the governing equations.

1. Basics of the CFD-KTGF Model

The governing equations can be expressed as follows:

The continuity equation:

$$\frac{\partial}{\partial t}(\alpha_q \rho_q) + \nabla \cdot (\alpha_q \rho_q \vec{v}_q) = 0,\ q = l, s,\ \alpha_l + \alpha_s = 1 \tag{4}$$

Momentum equations:

$$\frac{\partial}{\partial t}(\alpha_l \rho_l \vec{v}_l) + \nabla \cdot (\alpha_l \rho_l \vec{v}_l \vec{v}_l) = -\alpha_l \nabla p + \nabla \cdot \bar{\bar{\tau}}_l + K_{sl}(\vec{v}_s - \vec{v}_l) + \alpha_l \rho_l \vec{g} + \vec{F}_{lift,1} \tag{5}$$

$$\frac{\partial}{\partial t}(\alpha_s \rho_s \vec{v}_s) + \nabla \cdot (\alpha_s \rho_s \vec{v}_s \vec{v}_s) = -\alpha_s \nabla p - \nabla p_s + \nabla \cdot \bar{\bar{\tau}}_s + K_{sl}(\vec{v}_l - \vec{v}_s) + \alpha_s \rho_s \vec{g} + \vec{F}_{lift,s} \tag{6}$$

$$\bar{\bar{\tau}}_q = \alpha_q \mu_q (\nabla \vec{v}_q + \nabla \vec{v}_q^T) + \alpha_q \left(\lambda_q - \frac{2}{3}\mu_q\right) \nabla \cdot \vec{v}_q \bar{\bar{I}} \tag{7}$$

where $\bar{\bar{\tau}}_q$ is the stress tensor. Note that solid pressure and viscosity are physical concepts in the continuous phase. In this regard, Lun et al. [36] introduced granular temperature in the kinetic theory of gases and derived the KTGF model to consider the conservation of energy in the solid phase. The granular temperature equation can be expressed as follows:

$$\frac{3}{2}\left[\frac{\partial}{\partial t}(\alpha_s \rho_s \Theta_s) + \nabla \cdot (\alpha_s \rho_s \vec{v}_s \Theta_s)\right] = \nabla \cdot (\kappa_{\Theta_s} \nabla \Theta_s) + (-p_s I + \bar{\bar{\tau}}_s) : \nabla \vec{v}_s - \gamma_{\Theta_s} - 3K_{ls}\Theta_s \tag{8}$$

$$\kappa_{\Theta_s} = \frac{15 d_s \rho_s \alpha_s \sqrt{\Theta_s \pi}}{4(41-33\eta)}\left[1 + \frac{12}{5}\eta^2(4\eta - 3\alpha_s g_0) + \frac{16}{15\pi}(41-33\eta)\eta\alpha_s g_0\right] \tag{9}$$

$$\gamma_{\Theta_s} = \frac{12(1-e_{ss}^2) g_0}{d_s \sqrt{\pi}} \rho_s \alpha_s^2 \Theta_s^{1.5} \tag{10}$$

$$\eta = 0.5(1 - e_{ss}) \tag{11}$$

$$g_0 = [1 - (\alpha_s / \alpha_{s,max})^{1/3}]^{-1} \tag{12}$$

The main physical properties of the solid phase can be obtained using the following equations:

Pressure:

$$p_s = \alpha_s \rho_s \Theta_s + 2\rho_s (1 + e_{ss}) \alpha_s^2 g_0 \Theta_s \tag{13}$$

Shear viscosity:

$$\mu_s = \mu_{s,col} + \mu_{s,kin} + \mu_{s,fr} \tag{14}$$

$$\mu_{s,col} = \frac{4}{5}\alpha_s \rho_s d_s g_0 (1 + e_{ss})\left(\frac{\Theta_s}{\pi}\right)^{0.5} \tag{15}$$

$$\mu_{s,kin} = \frac{5 d_s \rho_s \sqrt{\Theta_s \pi}}{48 \alpha_s (1 + e_{ss}) g_0}\left[1 + \frac{4}{5}(1 + e_{ss})\alpha_s g_0\right]^2 \tag{16}$$

$$\mu_{s,fr} = \frac{p_s \sin\theta}{2\sqrt{I_{2D}}} \tag{17}$$

Bulk viscosity:

$$\lambda_s = \frac{4}{3} d_s \rho_s \alpha_s g_0 (1 + e_{ss})\left(\frac{\Theta_s}{\pi}\right)^{0.5} \tag{18}$$

2. Turbulent Model

In the studied cases, the superficial liquid velocity and the particle size are limited to 0.425 m/s and 0.8 mm, respectively. Subsequently, the Reynolds number is Re<50 and the flow is in the transitional regime. For this flow regime, Menter [37] developed a shear-stress transport (SST) k-ω to calculate the turbulent viscosity. This can be mathematically expressed in the form below:

$$\frac{\partial}{\partial t}(\alpha_l \rho_l k) + \frac{\partial}{\partial x_i}(\alpha_l \rho_l k \vec{v}_l) = \frac{\partial}{\partial x_j}\left(\Gamma_k \frac{\partial k}{\partial x_j}\right) + \alpha_l (G_k - Y_k + S_k) \tag{19}$$

$$\frac{\partial}{\partial t}(\alpha_l \rho_l \omega) + \frac{\partial}{\partial x_i}(\alpha_l \rho_l \omega v_l) = \frac{\partial}{\partial x_j}\left(\Gamma_\omega \frac{\partial \omega}{\partial x_j}\right) + \alpha_l (G_\omega - Y_\omega + D_\omega + S_\omega) \tag{20}$$

where the parameters k and ω can be obtained from Eqs. (19) and (20). Based on these parameters, the turbulent viscosity is defined as:

$$\mu_t = \alpha^* \frac{\rho k}{\omega} \tag{21}$$

where α^* is low Reynolds number correction factor:

$$\alpha^* = \alpha_\infty^* \left(\frac{0.024 + Re_t/6}{1 + Re_t/6}\right) \tag{22}$$

$$Re_t = \frac{\rho k}{\mu \omega} \tag{23}$$

3. Interphase Force Models

Studies show that when the Reynolds number is small, the turbulence dispersion force and virtual mass force becomes negligible compared to other interphase forces such as drag and lift forces. Accordingly, the Gidaspow and Moraga models are applied to obtain drag and lift forces, respectively.

3-1. Standard Gidaspow Drag Force Model

The drag force can be obtained by the product of the momentum transfer coefficient K_{sl} and the slip velocity $(\vec{v}_l - \vec{v}_s)$ in the form below:

$$F_{sl} = K_{sl}(\vec{v}_l - \vec{v}_s) \tag{24}$$

where K_{sl} is a pressure drop-dependent parameter. Moreover, drag force between the liquid medium and solid particles depends on the spherical shape of particles and is calculated using the Gidaspow model [38]. This model is a combination of the Wen and Yu model [39] and the Ergun equations [40] and can be mathematically expressed in the form below:

$$K_{sl} = \begin{cases} K_{Wen\text{-}Yu} = \frac{3}{4} C_D \frac{\alpha_s \alpha_l \rho_l |\vec{v}_s - \vec{v}_l|}{d_s} \alpha_l^{-2.65} & \alpha_l > 0.8 \\ K_{Ergun} = 150 \frac{\alpha_s (1-\alpha_l)\mu_l}{\alpha_l d_s^2} + 1.75 \frac{\rho_l \alpha_s |\vec{v}_s - \vec{v}_l|}{d_s} & \alpha_l \le 0.8 \end{cases} \tag{25}$$

$$C_D = \begin{cases} \frac{24}{Re_s}[1 + 0.15(Re_s)^{0.687}] & Re_s \le 1{,}000 \\ 0.44 & Re_s > 1{,}000 \end{cases} \tag{26}$$

$$Re_s = \frac{\alpha_l d_s \rho_l |\vec{v}_s - \vec{v}_l|}{\mu_l} \tag{27}$$

3-2. Modified Gidaspow Drag Force Model

The modified Gidaspow model [38,40] was developed for non-spherical particles and can be expressed as follows [27]:

$$K_{sl} = \begin{cases} K_{Wen\text{-}Yu\text{-}Haider} = \frac{3}{4} C_D \frac{\alpha_s \alpha_l \rho_l |\vec{v}_s - \vec{v}_l|}{d_s \psi} \alpha_l^{-2.65} & \alpha_l > 0.8 \\ K_{Ergun} = 150 \frac{\alpha_s (1-\alpha_l)\mu_l}{\alpha_l (d_s \psi)^2} + 1.75 \frac{\rho_l \alpha_s |\vec{v}_s - \vec{v}_l|}{d_s \psi} & \alpha_l \le 0.8 \end{cases} \tag{28}$$

where C_D can be estimated using the Haider and Levenspiel model [41], which is described as follows:

$$C_D = \begin{cases} \frac{24}{Re_s}(1 + b_1 Re_s^{b_2}) + \frac{b_3 Re_s}{b_4 + Re_s} & Re_s \le 1{,}000 \\ 0.44 & Re_s > 1{,}000 \end{cases} \tag{29}$$

$$b_1 = \exp(2.3288 - 6.4581\psi + 2.4486\psi^2) \tag{30}$$

$$b_2 = 0.0964 + 0.5565\psi \tag{31}$$

$$b_3 = \exp(4.905 - 13.8944\psi + 18.4222\psi^2 - 10.2599\psi^3) \tag{32}$$

$$b_4 = \exp(1.4681 + 12.254\psi - 20.7322\psi^2 + 15.8855\psi^3) \tag{33}$$

where ψ is the particle sphericity, which is set to 0.83 in this study.

3-3. Moraga Lift Force Model

In the momentum equation, the lift force ($\vec{F}_{lift}$), which is added to both phases, is defined as [42]:

$$\vec{F}_{lift,s} = -C_l \rho_l \alpha_s (\vec{v}_l - \vec{v}_s) \times (\nabla \times \vec{v}_l) \tag{34}$$

where C_b the lift coefficient, is defined as follows:

$$C_l = \begin{cases} 0.0767 & \varphi \le 6{,}000 \\ -(0.12 - 0.2e^{-\frac{\varphi}{3.6\times10^{-5}}})e^{-\frac{\varphi}{3\times10^{-7}}} & 6{,}000 < \varphi < 5\times10^7 \\ -0.6353 & \varphi > 5\times10^7 \end{cases} \tag{35}$$

where $\varphi = Re_s Re_w$, and Re_s and Re_w denote the Reynolds number based on the particle and vorticity, respectively.

$$Re_w = \frac{\rho_l (\nabla \times \vec{v}_l) d_s^2}{\mu_l} \tag{36}$$

4. Simulation Details

Fig. 1(b) shows the computational domain. ANSYS ICEM 19.0 software was employed to develop a 3D model with the same geometric parameters. The computational model was divided into the upper part (Part I) with structured elements and the lower part (Part II) with unstructured grids. The bottom of the fluidized bed with evenly arranged holes was used as a distribution plate. In this region, particles were initially patched with an initial height of H_0 (100 mm).

The imposed boundary conditions of the studied case are the velocity inlet, pressure outlet, and stationary walls with the no-slip condition for the liquid phase and Johnson and Jackson boundary conditions for the solid phase [43]. To simulate the complex turbulent flow, the SST k-ω model was applied to the liquid phase. Moreover, the second-order upwind scheme and SIMPLE algorithm were used to reach accurate results. The governing equations were solved using Fluent 2019 software. The pressure and momentum under-relaxation factors were set to 0.3 and 0.7, respectively. The time step and the convergence criterion were set to 0.001 s and 1×10^{-05}, respectively.

RESULTS AND DISCUSSION

1. Comparison between CFD Predictions and Experimental Data

In this section, the proposed CFD model is verified using experimental data. The comparative indicators are the bed expansion height and bed pressure drop at different particle sizes and superficial liquid velocities.

1-1. Bed Expansion

Studies reveal that expansion of the bed height is an important indicator in liquid-solid fluidized beds [44]. As mentioned above, fluidization experiments of spherical and irregular particles were performed. CFD simulations were carried out under the same liquid-solid fluidized bed structure parameters and the same operating conditions, and therefore the simulation results can be compared with experimental data.

Fig. 3 illustrates the distribution of the bed expansion ratio against the superficial liquid velocity, indicating a strong correlation between these two parameters. It is observed that as the superficial liquid velocity increases, the corresponding bed expansion rate increases. Meanwhile, it is found that the expansion rate of irregular particles is higher than that of spherical particles at the same superficial liquid velocity regardless of the particle size. Fig. 3(a) shows that for small particles with a size of 0.5±0.1 mm and a density of 2,670 kg/m^3, as the superficial liquid velocity increases from 0.017 m/s to 0.034 m/s, the expansion ratio of the spherical particle bed increases from 50% to 145%, while the expansion ratio of irregular-shaped particle bed under the same conditions increases from 70% to 190%. In Fig. 3(b) for large particles with a size of 0.7 mm and a density of 2,670 kg/m^3, the expansion ratio of a spherical particle bed in-

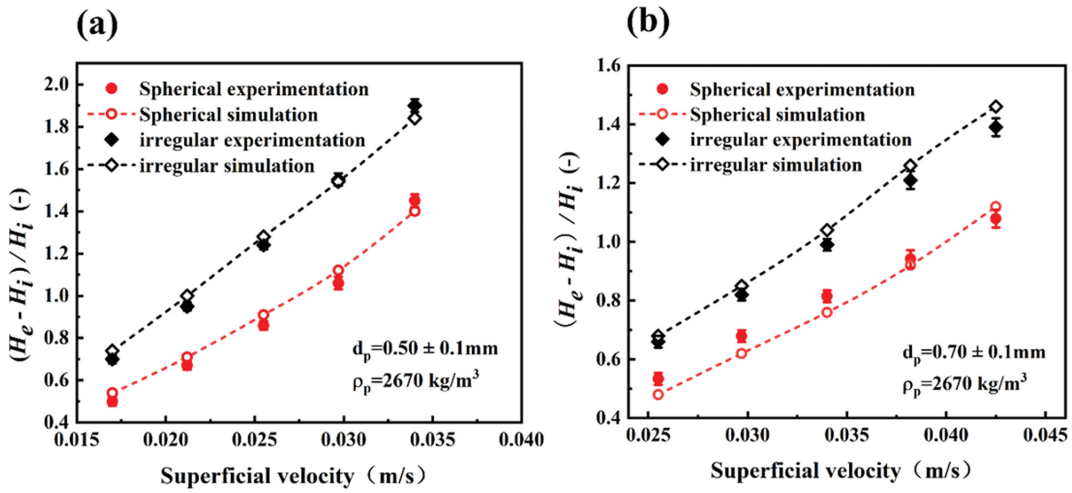

Fig. 3. Distribution of the bed expansion ratio against the superficial liquid velocity for spheres and irregular particles with density of 2,670 kg/m^3. (a) d_p=0.5±0.1 mm; (b) d_p=0.7±0.1 mm.

creases from 53% to 108%, while that of irregular-shaped particle bed increases from 66% to 139%. This trend may be attributed to the larger drag force of irregular-shaped particles compared with spherical particles in the same environment, which increases the expansion ratio. The root mean square error (RMSE) reflecting the deviation degree between experimental and numerical data is defined as follows [21]:

$$\mathrm{RMSE}=\sqrt{\frac{1}{n}\sum_{1}^{n}(y_i-y_i')^2} \tag{37}$$

where y_i' is the numerical data of the bed expansion ratio at the superficial liquid velocity i, and y_i denotes the experimental value; n denotes the number of experiment. The RMSE between CFD predictions and experimental data of the bed expansion ratio for spherical and irregular particles with a particle size of 0.5±0.1 mm is 0.049 and 0.043, respectively. The RMSE of bed expansion ratio for spherical and irregular particles with a particle size of 0.7±0.1 mm is 0.048 and 0.047, respectively. Fig. 3 demonstrates that the performed simulations are in excellent consistency with the experiment and the relative error is less than 5%.

Understanding bed expansion is the key to evaluating the particle separation performance in a fluidized flotation cell. Fig. 4 shows the expansion height of a solid-liquid fluidized bed. The initial conditions reflect the concentration of solids in the bed and the flow of fluid through the bed. The particle diameter is 0.7±0.1 mm, the density is 2,670 kg/m^3, and the superficial liquid velocity is 0.034 m/s. The initial height and porosity are 0.1 m and 0.43, respectively. Fig. 4 shows the simulated bed expansion height and instantaneous concentration of particles in the bed at different times. It is observed that the heterogeneous flow structure (i.e., particle cluster) for the liquid-solid system appears only at the beginning of fluidization (0-3 s). As the flow progresses, the bed height increases. However, there is a nonlinear correlation between bed expansion heights and time. The obtained results reveal that a steady-state flow can be achieved after t=20 s. It is concluded that the performed simulations are in excellent consistency with the experiment, indicating the accuracy of the proposed CFD model.

When the fluidized bed reaches the quasi-steady-state condition, the time-average solid concentration can be calculated as:

$$\varepsilon_{s,i}=\Sigma_{t_1}^{t_2}\varepsilon_{s,i}(t)/(t_2-t_1) \tag{38}$$

where Δt denotes the time step and t_1 and t_2 are set to 20 and 40 s, respectively. For spherical particles, the predicted particle concentration using the Gidaspow drag model (i.e., 0.325) is slightly higher

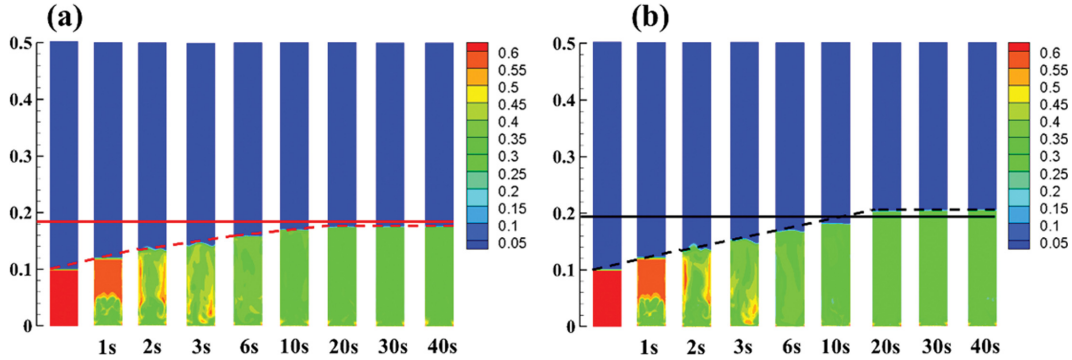

Fig. 4. Comparison of bed expansion heights of instantaneous particle concentration distribution at the superficial liquid velocity, v_L=0.034 m/s, d_p=0.7±0.1 mm and H_0=0.1 m. (a) spherical particles; (b) irregular particles.

than the experiment data (i.e., 0.316). Furthermore, for irregular particles, the predicted particle concentration using the modified Gidaspow drag model (i.e. 0.281) is slightly lower than the experiment data (i.e., 0.288). Accordingly, the relative error is 0.9%, which further validates the accuracy of the developed CFD model.

1-2. Pressure Drop

Bed pressure drop is another important factor in evaluating the hydrodynamic performance of the fluidized bed. When the flow passes through a particle bed, the flow pressure drops, which can be obtained through the following empirical equation [45,46]:

$$\Delta P = H_e(\rho_s - \rho_L)(1-\alpha_L)g \quad (39)$$

where H_e and α_L are the bed expansion height and the liquid volume fraction, respectively.

In this study, pressure drop was measured by experiment and also calculated by CFD simulation for different superficial liquid velocities and the obtained results are presented in Fig. 5. It is observed that for spherical particles, the pressure drop fluctuates greatly during the initial fluidization process. However, other particles with irregular shapes have less fluctuation. This may be attributed to a relatively large drag force in particles with an irregular shape, which leads to homogeneous fluidization. The CFD simulation and experimental values of the average pressure drop of spherical particles after 20 seconds are 943 and 939 Pa, respectively. These values for irregular particles are 944 and 934 Pa, respectively. It is concluded that the performed numerical simulation is in excellent consistency with the experiment.

2. Hydrodynamics Performance Characterization

This section analyzes the influence of affecting parameters, including the size and shape of particles, and superficial liquid velocity on the solid holdup, axial velocity, and particle temperature of the liquid-solid fluidization system.

2-1. Solid Holdup

The solid holdup is an important parameter in mineral processing. The higher the solid holdup, the higher the flow resistance to flow. In the present study, the influence of shape and size of particles on the axial velocity and solid holdup was studied using spherical and irregular particles of 0.5±0.1 mm and 0.7±0.1 mm. Fig. 6(a)

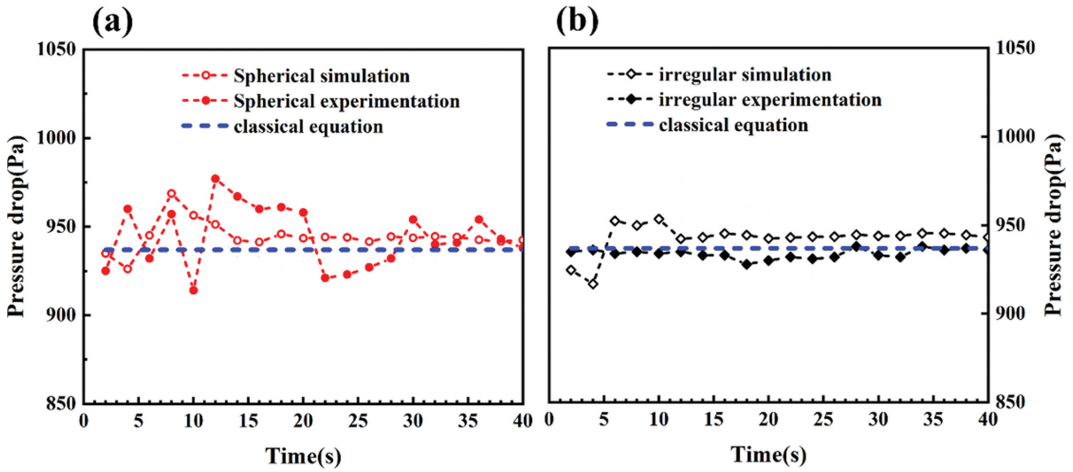

Fig. 5. Distribution of the pressure drop at a superficial liquid velocity of V_L=0.034 m/s and a particle size of d_p=0.7±0.1 mm with (a) spherical particles, and (b) irregular particles.

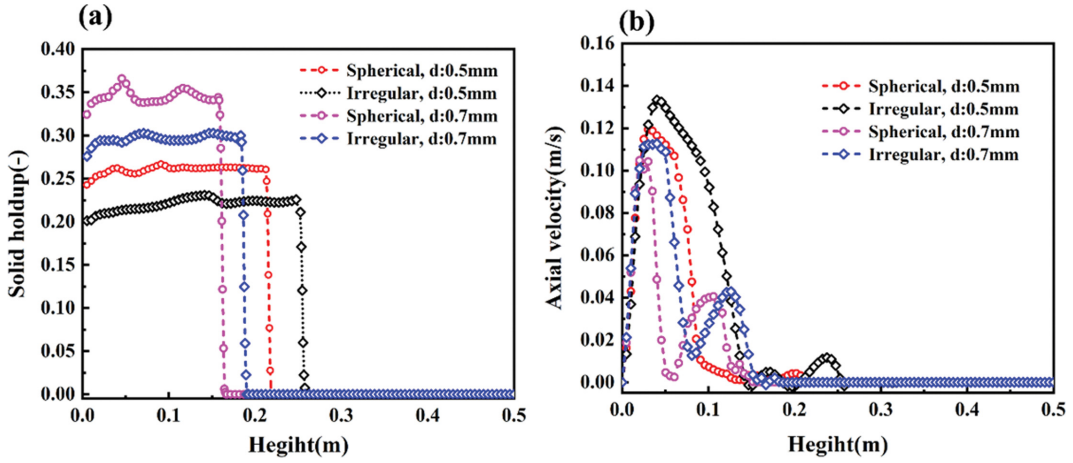

Fig. 6. Distributions of the solid holdup (a) and axial velocity (b) of spherical and irregular particles at a superficial liquid velocity of V_L= 0.0297 m/s.

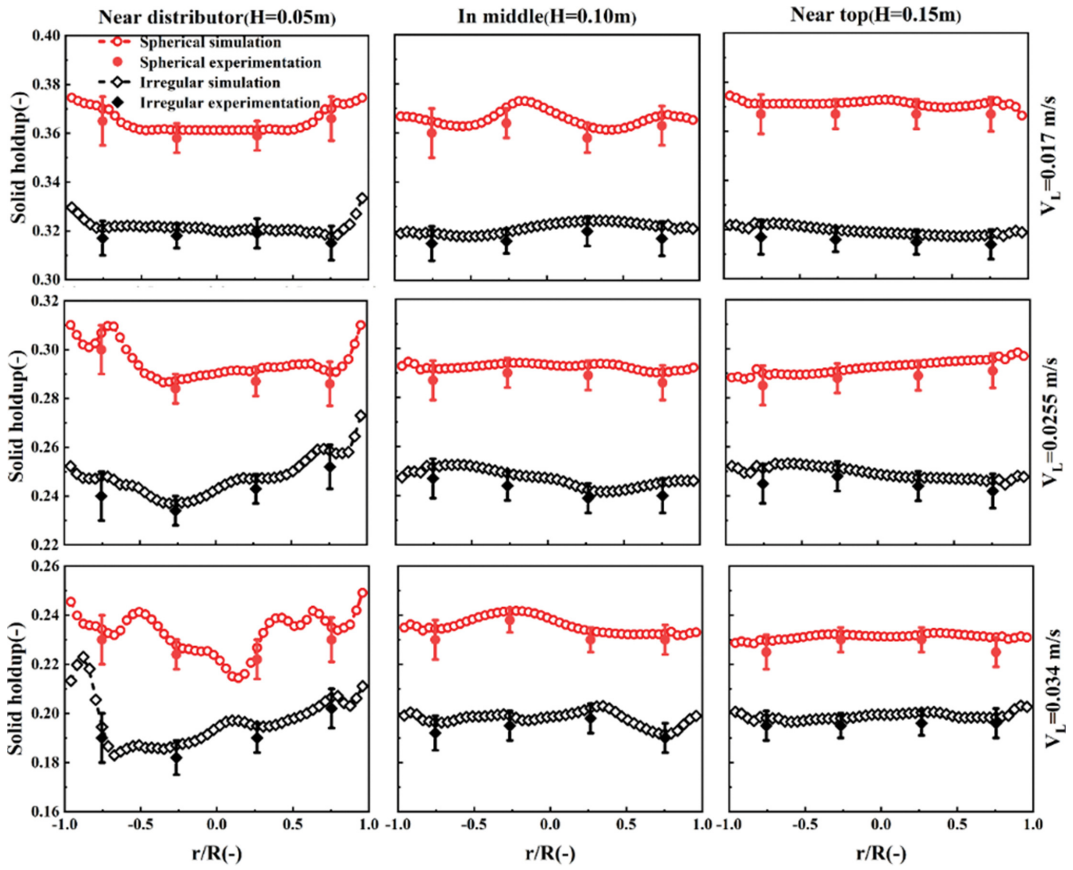

Fig. 7. Distributions of the solid holdup at different superficial liquid velocities and column heights.

shows the distribution of solid holdup at two particle shapes and two particle sizes, indicating that as the particle size decreases, the solid holdup also decreases. Rahaman et al. found that struvite pellets with larger particle size had a lower expansion index, indicating a higher retention rate at the same liquid velocity [47]. Moreover, it is found that the solid holdup of spherical particles is higher than that of irregular-shaped particles under the same particle size. The difference mainly originates from different bed heights. Fig. 6(b) shows the axial velocity distribution of two particle shapes with different particle sizes. In contrast to the solid holdup curve, the solid axial velocity shows an opposite trend. It is observed that low particle velocity and high solid holdup at the same superficial liquid velocity can be achieved using large spherical particles. Meanwhile, small irregular particles will gain high particle velocities and low solid holdup. The reason is that although the same energy is input through the upstream flow, the smaller particles will gain higher velocities compared to the larger particles [48].

Fig. 7 illustrates the radial distribution of mean solid holdup at different superficial liquid velocities and bed heights. It is observed that at a relatively low superficial liquid velocity (V_L=0.017 m/s), the solid holdup is evenly distributed in the middle and top of the bed for both spherical and irregular particles, but it is not evenly distributed at the bottom of the bed (H=0.05 m) and the solid holdup near the wall is larger than that at the central area (−0.75<r/R< 0.75). Moreover, it is found that as the superficial liquid velocity increases to 0.0255 and 0.034 m/s, the heterogeneous behavior for solid holdup continues to increase at the bottom of the bed. This phenomenon has also been reported before [49]. However, the particle distribution in the middle (H=0.10 m) and top (H=0.15 m) of the bed is more uniform even at high superficial liquid velocity. Generally, it is inferred that the solid holdup of the fluidized bed with irregular particles is smaller than that with spherical particles. This difference is attributed to the high fluid resistance caused by irregular particles [50].

2-2. Particle Axial RMS Velocity

Fig. 8(a) and 8(b) show the axial RMS velocity distributions of spherical and irregular particles in the bed at different superficial liquid velocities (V_L=0.0255, 0.0297, and 0.0425 m/s). It is observed that as the superficial velocity increases, the axial RMS velocity of particles increases. Meanwhile, the axial RMS velocity of irregular particles is greater than that of spherical particles, which may be attributed to the higher drag force of irregular particles. Fig. 8(c) shows the axial RMS velocity distribution of particles against the axial height, indicating that as the expansion height increases, the particle axial RMS velocity increases abruptly first and then reduces gradually. When V_L=0.0255 m/s, the axial RMS velocity of irregular particles and spherical particles has the same trend and the peak value occurs at h/H=0.05. However, the difference gradually increases as the superficial velocity increases. The peak value increases and both curves move to the right. When V_L increases to 0.0425 m/s, the peak values occur at h/H=0.15. As reported by Islam et al., the peak of RMS velocity indicates the location of the strong circula-

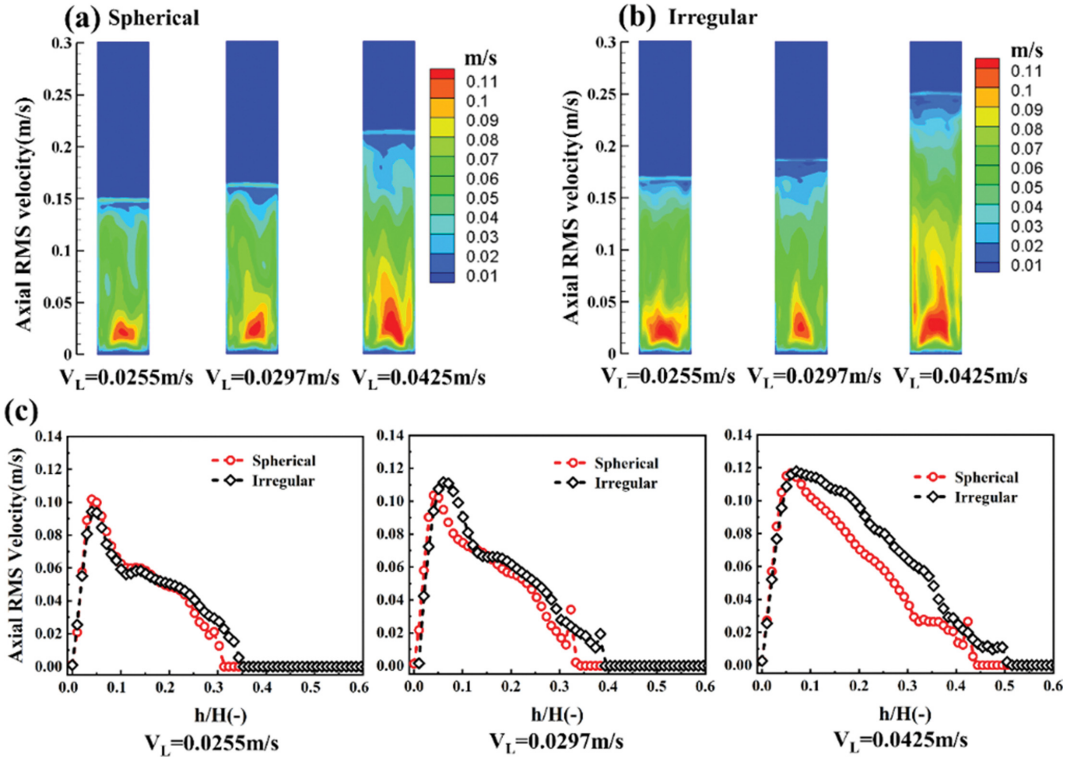

Fig. 8. Distributions of particle axial RMS velocity with different inlet superficial liquid velocities: (a) spherical particles; (b) irregular particles; (c) in relation to the dimensionless axial height.

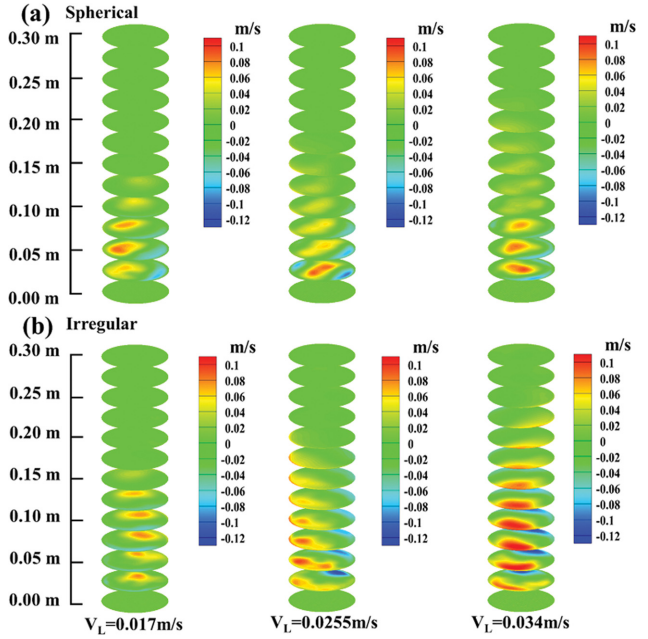

Fig. 9. Contours of the time-averaged axial velocity of the particle phase at different inlet superficial liquid velocities: (a) spherical particles; (b) irregular particles.

tion [51], as shown in Fig. 9, where h/H=0.15 (i.e., 0.075 m height) can also be observed in the cloud image of irregular particles on the right. It is inferred that the superficial liquid velocity can be used to directly regulate the axial velocity of particles in a fluidized bed reactor and control the fluidization.

Superficial liquid velocity strongly affects the flow behavior of particles during fluidization. Fig. 9 shows the contour lines of the time average axial velocity distribution of spherical and irregular particles in the bed at different superficial liquid velocities at the inlet (V_L=0.0017, 0.0255 and 0.034 m/s). The first column on the left shows that at V_L=0.0017 m/s, the axial velocity of irregular particles is relatively faster and the expansion height is 0.05 m higher than that of spherical particles. At V_L=0.0255 m/s, the velocities of spherical and irregular particles become unevenly distributed, extending from the central region to the wall region. Also, high particle axial velocities (red) are observed throughout the column, while low particle axial velocities (blue) are observed near the wall for spherical and irregular particles (middle column). When V_L increases to 0.034 m/s, the velocities of spherical and irregular particles become more unevenly distributed and move upward.

2-3. Granular Temperature

The particle granular temperature is an indicator to measure the collision intensity between particles and particle motion. When the volume fraction of particles is low, the number of particle collisions is relatively small and the granular temperature is low. Due to the short mean free path, granular temperature is also very low at high volume fraction [52].

Fig. 10 shows the time average of particle granular temperature at different column heights and superficial liquid velocities. In the axial direction, the kinetic energy of particles at the bottom of the bed (H=0.05 m) is higher than that at the other two positions (H=

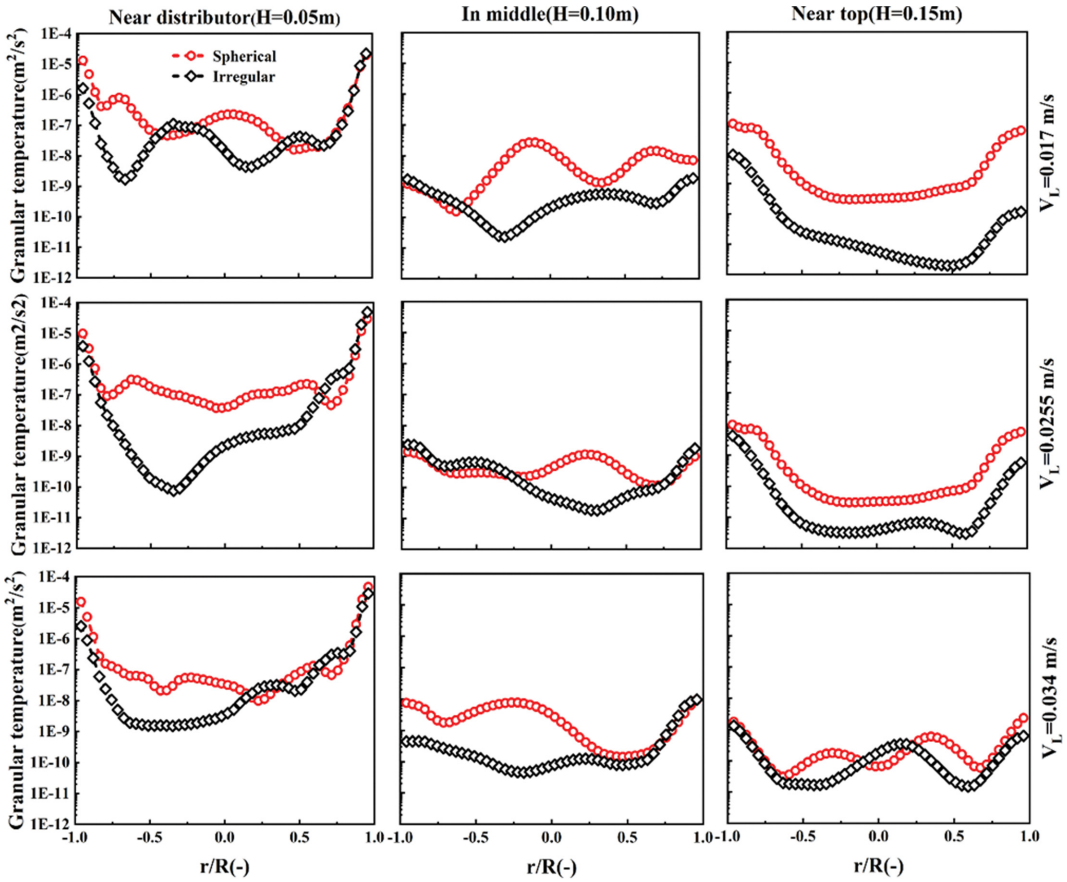

Fig. 10. Distribution of particle kinetic energy of spherical and irregular particles at different column height and superficial liquid velocities.

0.1 m and 0.15 m). The particle granular temperature near the wall is higher than that in the middle area (i.e., $-0.75<r/R<0.75$). The granular temperature of irregular particles is lower than that of spherical particles. The reason is that the particle velocity has less fluctuation due to the high fluid resistance originating from irregular particles [50]. When the superficial liquid velocity increases from V_L=0.017 m/s to 0.034 m/s, the granular temperature difference between spherical particles and irregular particles (i.e., H=0.15 m) approaches gradually. When the velocity is high, the particle distribution is more uniform and the influence of particle irregularity is weakened.

CONCLUSION

The hydrodynamic characteristics of spherical and irregular particles in a liquid-solid fluidized bed were studied. CFD simulation was carried out using the Euler-Euler method, and SST k-ω and KTGF models, and the obtained results were verified by experimental data. Then the influence of different parameters, including the size and shape of particles, and the superficial liquid velocity on fluidization characteristics was investigated. Based on the obtained results, the main conclusions can be summarized as follows:

The calculated bed expansion and pressure drop for spherical and irregular particles agree well with the experimental data, and the RMSE between them is less than 0.05.

At the same superficial liquid velocity of 0.0297 m/s, large particles of 0.7±0.1 mm can gain lower particle velocity (Vs=0.10 m/s) and higher solid holdup. On the contrary, irregular particles as small as 0.5±0.1 mm will obtain higher particle velocity (Vs=0.14 m/s).

At a relatively low superficial liquid velocity (V_L=0.017 m/s), the solid holdup is evenly distributed in the middle and top of the bed for both spherical and irregular particles, while it is not evenly distributed at the bottom of the bed (H=0.05 m) and the solid holdup near the wall is larger than that at the central area ($-0.75<r/R<0.75$).

As the superficial velocity increases continuously, the axial RMS velocity increases sharply at first and then decreases gradually. Irregular particles have a higher axial RMS velocity than spherical particles. The bed height h/H=0.15 is the position of strong circulation, where the RMS velocity is the peak value.

The granular temperature near the distributor (H=0.05 m) is higher than that in the middle and top of the column (H=0.1 m and 0.15 m) along the axial direction. Meanwhile, the particle granular temperature near the wall is higher than that in the middle region (i.e., $-0.75<r/R<0.75$) along the radial direction. Compared with spherical particles, irregular particles have a lower granular temperature due to the high fluid resistance originating from irregular particles.

ACKNOWLEDGEMENTS

This research was supported by the National Natural Science

Foundation of China (NSFC) (No. 52122406) and Hunan High-tech Industry Technology Innovation Leading plan (No. 2022GK4056).

NOMENCLATURE

C_D : drag coefficient
C_l : lift force coefficient
d_s : diameter of particles [m]
e : particle-particle restitution coefficient
D : diffusion coefficient [$m^2 \cdot s^{-1}$]
$\vec{F}$: the liquid-solid interphase force [$N \cdot m^{-3}$]
$\vec{g}$: gravitational acceleration [$m \cdot s^{-2}$]
g_0 : radial distribution function
G_i : the product term in turbulence model
H : bed expansion height [m]
I : unit tensor
k : turbulence kinetic energy [$m^2 \cdot s^{-2}$]
k_Θ : diffusion coefficient [$m^2 \cdot s^{-1}$]
K_{sl} : interphase exchange coefficient [$kg \cdot m^2 \cdot s^{-1}$]
N_c : courant number
p : pressure [Pa]
Re : Reynolds number
S_i : source term in the turbulence model
t : time [s]
v : velocity [$m \cdot s^{-1}$]
Y_i : dissipation terms in the turbulence model

Greek Letters

α : volume fraction
ρ : density [$kg \cdot m^{-3}$]
$\bar{\bar{\tau}}$: stress tensor [Pa]
μ : viscosity [Pa·s]
ε : voidage
Θ : granular temperature [$m^2 \cdot s^{-2}$]
λ_s : solid bulk viscosity [Pa·s]
ω : specific dissipation rate [s^{-1}]
κ : thermal conductivity [$W \cdot m^{-1} K^{-1}$]
η : efficiency of energy transfer from the liquid phase to the solid phase [%]
γ : the collisional dissipation energy [$kg \cdot m^{-1} s^{-3}$]
χ : bed expansion ratio

REFERENCES

1. N. Epstein, *Int. J. Chem. React. Eng.*, **1** (2002).
2. G. J. Jameson, L. Cooper, K. K. Tang and C. Emer, *Miner. Eng.*, **146** (2020).
3. B. Liu, X. Li, Z. Li, H. Sui and H. Li, *Chem. Eng. Res. Des.*, **94**, 501 (2015).
4. D. Shun, J.-S. Shin, D.-H. Bae, H.-J. Ryu and J. Park, *Korean J. Chem. Eng.*, **34**, 3125 (2017).
5. H. W. Lee, H. Jeong, Y.-M. Ju and S. M. Lee, *Korean J. Chem. Eng.*, **37**, 1174 (2020).
6. L. Q. Lu, K. Yoo and S. Benyahia, *Ind. Eng. Chem. Res.*, **55**, 10477 (2016).
7. R. Sowmeyan and G. Swaminathan, *Bioresour. Technol.*, **99**, 6280 (2008).
8. K. M. Qureshi, A. N. K. Lup, S. Khan, F. Abnisa and W. M. A. W. Daud, *Korean J. Chem. Eng.*, **38**, 1797 (2021).
9. D. Georges-Filteau, J. Bouchard and A. Desbiens, *IFAC-PapersOnLine*, **52**, 66 (2019).
10. S. Fosu, B. Awatey, W. Skinner and M. Zanin, *Miner. Eng.*, **77**, 137 (2015).
11. J. N. Kohmuench, M. J. Mankosa, H. Thanasekaran and A. Hobert, *Miner. Eng.*, **121**, 137 (2018).
12. J. N. Kohmuench, M. J. Mankosa, E. S. Yan, H. Wyslouzil and L. Christodoulou, 2065 (2010).
13. B. Awatey, H. Thanasekaran, J. N. Kohmuench, W. Skinner and M. Zanin, *Miner. Eng.*, **50**, 99 (2013).
14. T.-W. Cheng and P. N. Holtham, *Miner. Eng.*, **8**, 883 (1995).
15. H. Soto and G. Barbery, *Mining Metall. Explor.*, **8**, 16 (1991).
16. S. V. Ghatage, Z. Peng, M. J. Sathe, E. Doroodchi, N. Padhiyar, B. Moghtaderi, J. B. Joshi and G. M. Evans, *Chem. Eng. J.*, **256**, 169 (2014).
17. A. Tripathy, S. Bagchi, S. K. Biswal and B. C. Meikap, *Chem. Eng. Res. Des.*, **117**, 520 (2017).
18. A. Tripathy, A. K. Sahu, S. K. Biswal and B. K. Mishra, *Particuology*, **11**, 789 (2013).
19. O. J. I. Kramer, P. J. de Moel, J. T. Padding, E. T. Baars, Y. M. F. E. Hasadi, E. S. Boek and J. P. van der Hoek, *J. Water Process Eng.*, **37**, 101481 (2020).
20. O. J. I. Kramer, J. T. Padding, W. H. van Vugt, P. J. de Moel, E. T. Baars, E. S. Boek and J. P. van der Hoek, *Int. J. Multiphase Flow*, **127** (2020).
21. J. Peng, W. Sun, H. Han and L. Xie, *Minerals*, **11**, 569 (2021).
22. J. T. Cornelissen, F. Taghipour, R. Escudie, N. Ellis and J. R. Grace, *Chem. Eng. Sci.*, **62**, 6334 (2007).
23. G. Liu, P. Wang, H. Lu, F. Yu, Y. Zhang, S. Wang and L. Sun, *Particuology*, **25**, 42 (2016).
24. H. Luo, C. Zhang and J. Zhu, *Powder Technol.*, **348**, 93 (2019).
25. B. Pang, S. Wang, W. Chen, M. Hassan and H. Lu, *Powder Technol.*, **366**, 249 (2020).
26. P. W. Lau, R. Utikar, V. Pareek, S. Johnson, S. Kale and A. Lali, *Chem. Eng. Res. Des.*, **91**, 1660 (2013).
27. Y. He, S. Yan, T. Wang, B. Jiang and Y. Huang, *Powder Technol.*, **287**, 264 (2016).
28. H. P. Zhu, Z. Y. Zhou, R. Y. Yang and A. B. Yu, *Chem. Eng. Sci.*, **63**, 5728 (2008).
29. L. M. Armstrong, S. Gu and K. H. Luo, *Int. J. Heat Mass Tran.*, **53**, 4949 (2010).
30. C. Loha, H. Chattopadhyay and P. K. Chatterjee, *Chem. Eng. Sci.*, **75**, 400 (2012).
31. H. Lu, H. Yurong and D. Gidaspow, *Chem. Eng. Sci.*, **58**, 1197 (2003).
32. A. Neri and D. Gidaspow, *AIChE J.*, **46**, 52 (2000).
33. J. Wang, W. Ge and J. Li, *Chem. Eng. Sci.*, **63**, 1553 (2008).
34. F. Dioguardi, P. Dellino and D. Mele, *Powder Technol.*, **260**, 68 (2014).
35. L. Hua, H. Zhao, J. Li, J. Wang and Q. Zhu, *Powder Technol.*, **284**, 299 (2015).
36. C. K. K. Lun, S. B. Savage, D. J. Jeffrey and N. Chepurniy, *J. Fluid Mech.*, **140**, 223 (1984).
37. F. R. Menter, *Aiaa J.*, **32**, 1598 (1994).

38. D. Gidaspow, *Multiphase flow and fluidization: continuum and kinetic theory descriptions*, Academic press, New York (1994).
39. C. Y. Wen, *Chem. Eng. Prog. Symp. Ser.*, **62**, 100 (1962).
40. S. Ergun, *Chem. Eng. Prog.*, **48**, 89 (1952).
41. A. Haider and O. Levenspiel, *Powder Technol.*, **58**, 63 (1989).
42. F. J. Moraga, F. J. Bonetto and R. T. Lahey, *Int. J. Multiphase Flow*, **25**, 1321 (1999).
43. P. C. Johnson and R. Jackson, *J. Fluid Mech.*, **176**, 67 (1987).
44. A. A. Avidan and J. Yerushalmi, *Powder Technol.*, **32**, 223 (1982).
45. A. Singh, R. Verma, K. Kishore and N. Verma, *Chem. Eng. Process*, **47**, 957 (2008).
46. L. M. Romeo, L. I. Díez, I. Guedea, I. Bolea, C. Lupiáñez, A. González, J. Pallarés and E. Teruel, *Exp. Therm. Fluid Sci.*, **35**, 477 (2011).
47. M. S. Rahaman, D. S. Mavinic and N. Ellis, *J. Environ. Eng. Sci.*, **9**, 137 (2014).
48. Z. Ye, Y. Shen, X. Ye, Z. Zhang, S. Chen and J. Shi, *J. Environ. Sci.*, **26**, 991 (2014).
49. J. Peng, W. Sun, L. Xie, H. Han and Y. Xiao, *Minerals*, **12** (2022).
50. M. T. Islam and A. V. Nguyen, *Miner. Eng.*, **134**, 176 (2019).
51. M. T. IslamIslam and A. V. Nguyen, *Chem. Eng. Res. Des.*, **159**, 13 (2020).
52. G. Liu, P. Wang, S. Wang, L. Sun, Y. Yang and P. Xu, *Adv. Powder Technol.*, **24**, 537 (2013).